ADVANCED FUNCTIONAL MATERIALS
www.afm-journal.de

Efficient Ag@AgCl Cubic Cage Photocatalysts Profit from Ultrafast Plasmon-Induced Electron Transfer Processes

Yuxin Tang, Zhelong Jiang, Guichuan Xing, Anran Li, Pushkar D. Kanhere, Yanyan Zhang, Tze Chien Sum, Shuzhou Li,* Xiaodong Chen, Zhili Dong,* and Zhong Chen**

Photon-coupling and electron dynamics are the key processes leading to the photocatalytic activity of plasmonic metal-semiconductor nanohybrids. To better utilize and explore these effects, a facile large-scale synthesis route to form Ag@AgCl cubic cages with well-defined hollow interiors is carried out using a water-soluble sacrificial salt-crystal-template process. Theoretical calculations and experimental probes of the electron transfer process are used in an effort to gain insight into the underlying plasmonic properties of the Ag@AgCl materials. Efficient utilization of solar energy to create electron-hole pairs is attributed to the significant light confinement and enhancement around the Ag/AgCl interfacial plasmon hot spots and multilight-reflection inside the cage structure. More importantly, an ultrafast electron transfer process (≤150 fs) from Ag nanoparticles to the AgCl surface is detected, which facilitates the charge separation efficiency in this system, contributing to high photocatalytic activity and stability of Ag@AgCl photocatalyst towards organic dye degradation.

1. Introduction

Semiconductor materials play a vital role in a number of next-generation high-tech domains such as energy harvest-conversion and environmental applications including photocatalysis, photoelectrolysis, and photovoltaics.[1] To date, the development of highly active photocatalysts nanostructures for solar light absorption is still a bottleneck for practical applications. It is known that well-controlled hierarchical structures, particularly 3D structures, could provide high specific surface area with well-aligned pore structures that shorten the diffusion paths to active surface sites.[2] For example, the hierarchical structures of green leaves and certain photosynthetic plants are optimized for efficient light harvesting and sunlight conversion to chemical energy by photosynthesis.[2a,3] In photocatalytic or photovoltaic applications, similar structures can provide a means of improving photoenergy conversion efficiency due to the enhanced light harvesting, short charge-carrier transport paths, and increased active sites in porous micro/nanochannels.[4]

Inspired by the benefit of the hierarchical structure, the present work demonstrates the feasibility of using a water-soluble sacrificial salt-crystal-template (SCT) to assemble porous hierarchical nanostructures with hollow interior morphologies. The critical features in the success of the SCT route include proper selection and preparation of the template material, adequate shell growth, and proper dissolution of the core template afterwards. For proof of concept, sodium chloride (NaCl) is selected as the template for the production of AgCl cubic cages. NaCl is an ideal template material due to its low cost, abundance, and ease of removal via dissolution; hence the preparation cost is minimized for large scale industry applications. Following the same principle but varying the geometry and composition of the template, this SCT route could potentially be used to synthesize other types of porous functional materials.

Interestingly, when coupled with Ag nanoparticles, this unique AgCl cage possessed excellent photocatalytic activity and high stability, which is generally ascribed to the plasmonic effect of noble metals. Plasmonic noble-metal nanostructures (such as Au and Ag) are characterized by their strong interaction with photons through an excitation of surface plasmon resonance (SPR).[5] Recently, studies have indicated that silver/silver compounds (Ag@AgX, X = Cl, Br, I, O, etc.) possess excellent photocatalytic activity and high stability due to the SPR effect of noble metal nanoparticles under various light irradiations.[6] The coupling of semiconductor and metal nanoparticles provides a unique pathway for the discharge of electrons at the electrolyte interface.[7] Earlier studies[6a,6b,6d,6h]

Dr. Y. Tang, Z. Jiang, A. Li, Dr. P. D. Kanhere, Dr. Y. Zhang, Prof. S. Li, Prof. X. Chen, Prof. Z. Dong, Prof. Z. Chen
School of Materials Science and Engineering
Nanyang Technological University
Singapore 639798, Singapore
E-mail: lisz@ntu.edu.sg; zldong@ntu.edu.sg; aszchen@ntu.edu.sg
Z. Jiang, Prof. T. C. Sum
C. N. Yang Scholars Programme
Nanyang Technological University
60 Nanyang Drive, SBS-02n-45
Singapore 637551, Singapore
E-mail: tzechien@ntu.edu.sg
Dr. G. Xing
Division of Physics and Applied Physics
School of Physical and Mathematical Sciences
Nanyang Technological University
Singapore 637371, Singapore

DOI:10. 1002/adfm.201203379

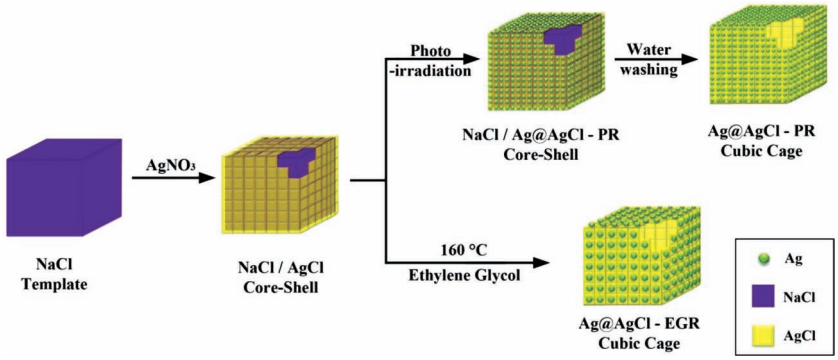

Scheme 1. Schematic illustration of the water-soluble sacrificial salt-crystal-template (SCT) route for the formation of Ag@AgCl cubic cages. Two methods have been selected to generate Ag NPs: photoreduction (PR) and ethylene glycol-assisted reduction (EGR). Note that in this scheme, AgCl or Ag@AgCl at one corner of each cube was deliberately deleted to reveal the inner constitutions of the cubes and cages.

suggested two main modes of electron transfer in silver/silver halides. In one mode, the SPR electrons remain in the Ag nanoparticles rather than being transferred to silver halides, which are expected to be directly trapped by O_2 to form the reactive oxygen radicals.[6a,6d] Another mode involves the SPR electrons transferring to the conduction bands of the silver halides.[6b,6h] Electron spin resonance and cyclic voltammetry analyses on the Ag-AgI/Al_2O_3 case support this opinion.[6b]

Despite these proposed electron dynamics in Ag@AgCl hybrid,[6a,6d] the exact electron transfer process is not yet clearly understood and direct experimental observation on it has been limited. With the aid of computer simulations and transient absorption spectroscopy, information about plasmonic electromagnetic hot spots and the plasmon-induced electron transfer processes in Ag@AgCl nanohybrid structures is obtained in this work. Specifically, the electronic transfer process between Ag nanoparticles and AgCl is identified to complete on an ultrafast timescale of less than 150 fs. Unraveling the mystery of these fundamental electronic events is a critical step towards elucidating the underlying mechanisms leading to the activity and stability of the Ag@AgX photocatalysts.

2. Results and Discussions

2.1. Synthesis and Characterization of Ag@AgCl Cubic Cages

Our design strategy, shown in **Scheme 1**, used a water soluble sacrificial salt-crystal-template (SCT) process to synthesize Ag@AgCl plasmonic photocatalysts with cubic cage morphology. The color change of reaction solution at different stages is shown in Figure S1 (Supporting Information). SCT NaCl templates were prepared by injecting saturated NaCl aqueous solution into anhydrous ethanol. The drastic decrease in NaCl solubility from water (26.4 wt% at 25 °C) to ethanol (0.05 wt% at 25 °C) resulted in the super-saturation of NaCl right after the instant of injection, and therefore, white colored NaCl crystals precipitated out immediately and assumed their thermodynamically stable cubic morphology. It is noted that other methods to generate NaCl crystals with different morphologies are also suitable for AgCl cage structure preparation. $AgNO_3$ was subsequently added into the NaCl dispersion, along with the assistance of surfactant PVP to prevent the aggregation of AgCl particle. Ion exchange diffusion reaction between NaCl and Ag^+ in the solution led to the heterogeneous nucleation and continued growth of AgCl on the surface of the NaCl template, evidenced from the color of the solution changing from yellow (Figure S1a, Supporting Information) to pale yellow (Figure S1b).

Figure 1a,b show field-emission scanning electron microscopy (FESEM) images of the NaCl/AgCl core-shell cubes. As can be seen, monodispersed NaCl/AgCl cubes (ca. 1.0–1.3 μm in edge length) were successfully produced with clearly defined edges. Figure 1c presents the transmission electron microscopy (TEM) image of an individual NaCl/AgCl cube. Compared with pure NaCl crystals (Figure S2, Supporting Information), the NaCl/AgCl samples show different contrast at the core and peripheral regions, typical for core-shell structured materials. It is expected that the brighter core was composed of NaCl, while the shell composed of AgCl appeared darker due to its larger mass. It is clearly visible from Figure 1c that each shell wall had relatively constant shell thickness with smooth outer and inner surfaces. The shell wall thickness is estimated from Figure 1c to be ca. 7% of the cube edge length. To further demonstrate the co-existence of NaCl and AgCl in these cubes, elemental mapping analysis and X-ray photoelectron spectroscopy (XPS) tests were carried out. The upper-left image in Figure 1d shows the SEM image of the regions where elemental mapping was performed. The magenta, yellow, and cyan colors in Figure 1d correspond to the mapping of chlorine, sodium and silver elements, respectively. It is observed that all three elements existed in the cubes, in agreement with the proposed NaCl/AgCl composition. Close scrutiny of Figure 1d reveals that Ag element was more concentrated at the periphery of the cubes; Na element was more concentrated at the centre; whereas Cl was uniformly distributed throughout the cube. The XPS survey spectrum (Figure 1e) of the NaCl/AgCl samples confirmed Na, Ag and Cl as the main components. Trace amount of C and O was also revealed. For Cl 2p (inset in Figure 1e), two peaks were observed at binding energies of about 197.8 and 199.8 eV, corresponding to Cl $2p_{3/2}$ and Cl $2p_{1/2}$, respectively. Also, the Ag 3d peaks at 367.8 and 373.8 eV can be assigned to the binding energies of Ag $3d_{5/2}$ and Ag $3d_{3/2}$, respectively.[6i] These observations further confirm the success of our template-assisted formation of NaCl/AgCl core-shell cubes. We have subjected some samples to a water dissolution step to demonstrate the feasibility of removing its sacrificial SCT core without losing the structural integrity of the shell. During this process, the water molecular can penetrate the AgCl shell and dissolute NaCl cores. The cubic cage morphology of AgCl was observed (Figure S3, Supporting Information), and the hollow interior of the cubic cages were accessible through the openings on the cage surfaces as in Figure S3a, or through the etched surface of the cube as in Figure S3b.

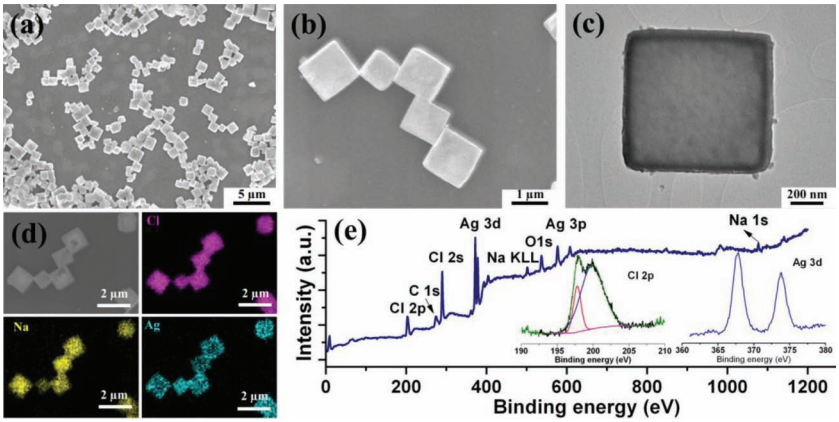

Figure 1. a,b) Typical FESEM images of NaCl/AgCl core-shell cubes. c) TEM image of an individual NaCl/AgCl core-shell cube. d) Energy dispersive X-ray (EDX) elemental mapping analysis of NaCl/AgCl core-shell cubes, showing the SEM image of the analysed sample, Cl element mapping (magenta), Na element mapping (yellow), and Ag element mapping (cyan). e) XPS spectrum of the NaCl/AgCl core-shell cubes. The insets in (e) are the high resolution XPS spectra of Cl 2p and Ag 3d.

Without the removal of the sacrificial core, two methods were employed for the deposition of Ag nanoparticles (NPs) on the NaCl/AgCl core-shell cubes (Scheme 1): photoreduction (PR) and ethylene glycol-assisted reduction (EGR). As shown in Scheme 1, for the PR method, free electrons generated upon illumination would combine with interstitial silver ions in AgCl lattice to form Ag NPs on the AgCl surface, and the colour of solution changed to purple (Figure S1c, Supporting Information). The product after photo-illumination was NaCl/Ag@AgCl core-shell cubes (NaCl/Ag@AgCl–PR), and the sacrificial NaCl core could be subsequently removed by water dissolution, leaving behind Ag@AgCl–PR cubic cages. For the EGR method, ethylene glycol was added into the NaCl/AgCl ethanolic suspension. Ethylene glycol is frequently employed as solvent[8] and/or reducing agent in the polyol process,[9] which is capable of reducing AgCl to form Ag NPs under direct heating[6d] or microwave heating.[10] Here, we used direct heating method, during which low boiling point ethanol evaporated and the suspension turned pale red (Figure S1d, Supporting Information). In addition, the NaCl core was mildly dissolved into the ethylene glycol media. Therefore, ethylene glycol played the role of reducing agent as well as sacrificial-core removing medium. **Figure 2**a shows a low magnification FESEM image of Ag@AgCl–EGR, illustrating the retention of cubic shape after the Ag NPs formation and sacrificial-core removal. Similar morphology was observed for Ag@AgCl–PR samples (not shown). Figure 2b and c provide high magnification FESEM images for Ag@AgCl–PR and Ag@AgCl–EGR, respectively. Openings on the surfaces (pointed by the arrows) were indicative of their hollow cage morphology. All features of cubic shape, hollow interior, and Ag NPs deposition can be observed from the TEM image of Ag@AgCl–PR (Figure 2d), which demonstrates that the porous AgCl outer shell was able to retain its three-dimensional cubic shape after the water-dissolution process. On the other hand, for Ag@AgCl–EGR, the hollow interior (Figure 2e) was not as obvious, probably because the high temperature EGR process promoted the growth of AgCl crystal, resulting in denser AgCl shell structure. Exposure of Ag@AgCl–EGR to prolonged electron beam bombardment could cause coagulation of the crystals in the shell, thereby revealing its hollow structure (Figure S4, Supporting Information).

The crystal structure of the products formed by the SCT process was investigated by X-ray diffraction (XRD) (Figure S5, Supporting Information). After shell growth, the coexistence of cubic phase NaCl and cubic phase AgCl was evidenced in Figure S5a (Supporting Information). As seen in Figure S5b (Supporting Information), during the PR route, when NaCl/AgCl was illuminated with light, cubic phase Ag was generated (inset of Figure S5), forming NaCl/Ag@AgCl. After water-dissolution, the as-prepared Ag@AgCl–PR had no NaCl peaks (Figure S5c, Supporting Information), indicating complete removal of sacrificial core. Similar observation was made in the Ag@AgCl–EGR after the EGR treatment (Figure S5d). However, no Ag peaks were observed in the XRD pattern for Ag@AgCl–EGR. This may be due to the low content and high dispersity of Ag formed during EGR process.[11] To further examine the chemical status of the products, XPS was conducted and the results were shown in Figure S6 (Supporting Information). Compared with the NaCl/AgCl sample, the Na 1s and Na KLL peaks disappeared in survey spectra (Figure S6A) of Ag@AgCl-PR and Ag@AgCl-EGR samples since the NaCl cores were removed, while the main components of Ag and Cl peaks were similar. High resolution XPS in Figure S6B indicated that the surface metallic Ag^0 content was ca. 1.3% for Ag@AgCl-PR, but lower for Ag@AgCl-EGR sample, which was consistent with the XRD results (Figure S5, Supporting Information).

UV-vis diffuse reflectance spectra of the various samples are shown in **Figure 3**, along with their corresponding digital photos. The absorption of UV light (below 390 nm) for NaCl/AgCl was due to large band gap energy of AgCl (indirect band gap: 3.25 eV, direct band gap: 5.15 eV), while the visible light absorption was very limited. Therefore, NaCl/AgCl core-shell cubes were white in colour. The limited absorption for NaCl/AgCl in the visible region might be due to the small amount of Ag^0 formed by room light illumination during preparation. After PR, the NaCl/Ag@AgCl–PR became purple and showed greatly increased absorption of light, especially in the visible region. This enhancement in light absorption was due to the localized surface plasmon resonance (SPR) and interband UV excitation of Ag NPs.[12] The broad SPR absorption had two peaks, one at around 550 nm and the other at around 730 nm. The visible absorption peak at 550 nm was much stronger for NaCl/Ag@AgCl–PR. When sacrificial-core was removed, the purplish NaCl/Ag@AgCl–PR changed to brownish Ag@AgCl–PR. As seen in Figure 3, Ag@AgCl–PR showed stronger and broader absorption both in the visible and UV regions. We speculate that such colour and absorption characteristic changes were associated with the internal multi-reflection of light-waves within the cage cavities of the

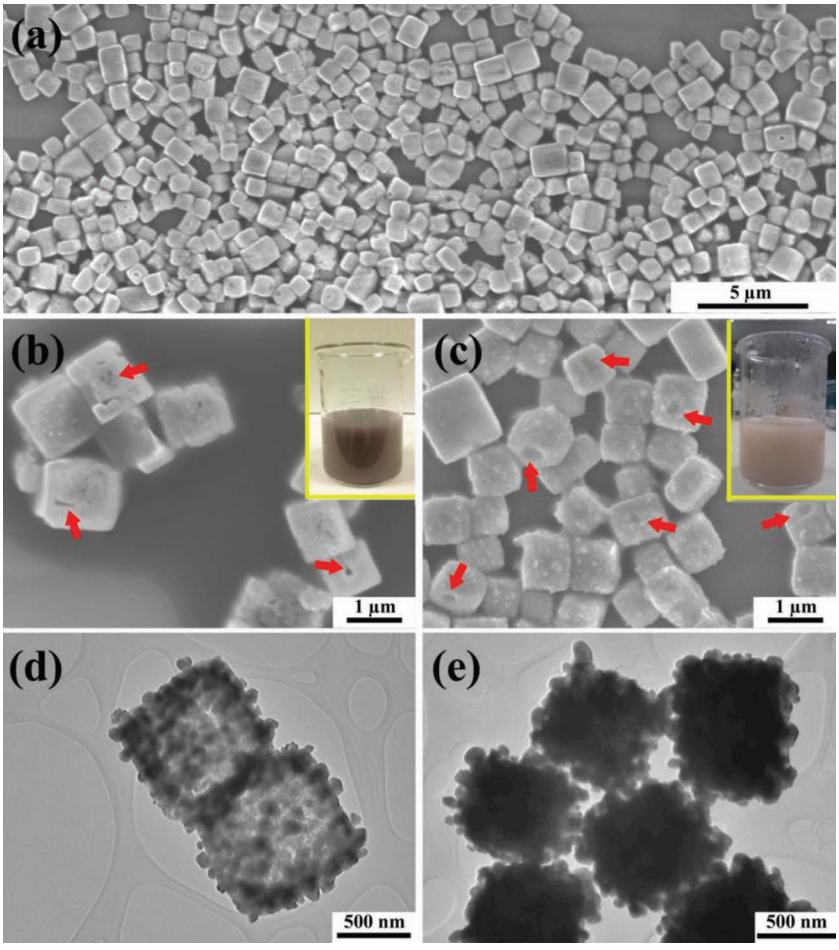

Figure 2. a) Typical FESEM image of Ag@AgCl–EGR at low magnification. Typical FESEM images of b) Ag@AgCl–PR and c) Ag@AgCl–EGR cubic cages at high magnifications. The arrows in (b) and (c) indicate the pore opening on the cage surface, showing the hollow interiors of the cubic cages. Typical TEM images of d) Ag@AgCl–PR and e) Ag@AgCl–EGR cubic cages. The digital photographs inset in (b) and (c) show the solutions of Ag@AgCl–PR and Ag@AgCl–EGR cubic cages, respectively.

porous AgCl (Figure 2d), whose model (purple color scheme) is shown in Figure 3. Such reflection-enhanced light-harvesting features are typical for hollow and porous materials structure[13] and have recently been identified to be responsible for the photocatalytic performance enhancement.[14] Ag@AgCl–EGR also exhibited broad visible light absorption and the hollow cage absorption characteristics afore-mentioned. However, the intensity of light absorption was somewhat lower. This could be attributed to its lower Ag^0 content and the more compacted AgCl shell (Figure 2e). The latter could decrease the light penetration into the cage, so the internal reflection enhanced light absorption effect was less prominent (model shown in Figure 3, red color scheme). In contrast to the higher peak at 550 nm for Ag@AgCl–PR, the absorption peak at 730 nm was stronger for Ag@AgCl–EGR, giving rise to its pale red appearance. The pale red color has been frequently reported for Ag@AgCl that has undergone reduction in ethylene glycol.[2d,6d] As the plasmonic absorption of metal NPs depends on their shape, size, mutual distance, and surrounding materials,[5,15] it is suspected here that the relatively high plasmon intensity at 730 nm for Ag@AgCl–EGR may result from shorter interparticle Ag NPs distances or/and larger sized Ag NPs generated by EGR processes in accordance with the primitive observation by FESEM and TEM images (Figure 2b–e) since previous research[14b,16] demonstrated that large particles size and short separation distances of novel metal nanoparticles will cause a red-shift in SPR absorption spectra.

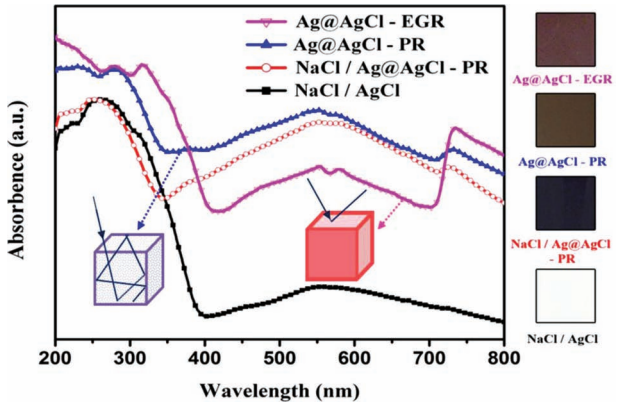

Figure 3. UV-vis absorption spectra of the as-prepared samples of NaCl/AgCl core-shell cubes, NaCl/Ag@AgCl–PR core-shell cubes, Ag@AgCl–PR, and Ag@AgCl–EGR. The digital photographs on the right are the corresponding colors. The inset schemes are the proposed models of light passage through the Ag@AgCl–PR and Ag@AgCl–EGR samples.

2.2. Photocatalytic Performance of Ag@AgCl Cubic Cages

The photocatalytic activities of the as-prepared Ag@AgCl samples were investigated by the degradation of methyl orange (MO) under visible light. Bulk form of Ag@AgCl was used for comparison. Its correspoding morphology, and UV-vis absorption spectra were provided in Figure S7 (Supporting Information). As can be seen in **Figure 4**a, both the cubic cages Ag@AgCl–PR and Ag@AgCl–EGR showed superior photocatalytic activity; they can nearly completely decompose 10 mg L^{-1} MO within 360 s of visible light irradiation while the bulk Ag@AgCl can only decompose 14% of MO during the same interval. Neither the photolysis experiment without photocatalyst nor the catalytic experiment without light irradiation showed any observable decrease in MO concentration with time, demonstrating that photocatalysis was indeed the cause for the decomposition of MO. Ag@AgCl–PR showed slightly higher activity than Ag@AgCl–EGR, probably because Ag@AgCl–PR had higher content of Ag^0, better absorption of visible light, and smaller Ag NPs with better

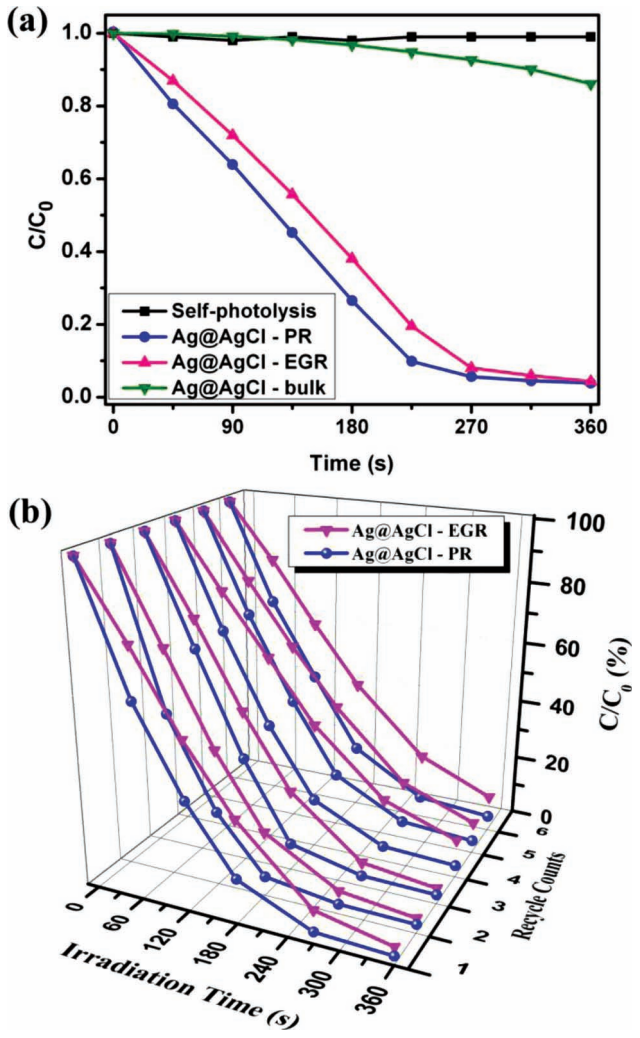

Figure 4. a) Photodegradation of methyl orange (MO) without and with the presence of as-prepared Ag@AgCl–PR, Ag@AgCl–EGR, and Ag@AgCl–bulk under visible light. C_0 is the initial concentration of MO aqueous solution (10 mg L^{-1}), and C is the instant concentration of MO solution during photodegradation. b) Recycling experiments of Ag@AgCl–PR and Ag@AgCl–EGR in the photodegradation of MO after their use in (a).

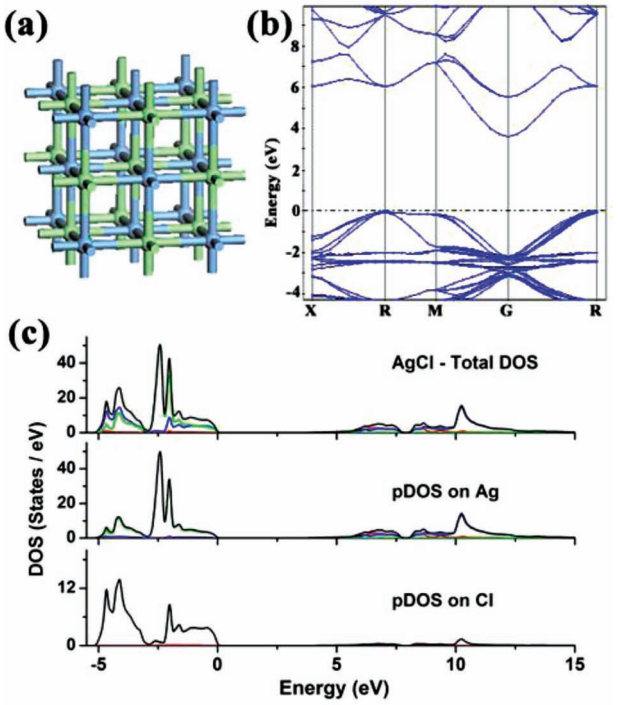

Figure 5. a) Unit cell of AgCl (space group No 225; Fm-3m) used in DFT calculations; b) energy-band diagram, and c) density of states for AgCl calculated by hybrid density functional method.

electron storage capacity and higher Fermi level.[7] Assuming a pseudo-first-order kinetics for MO degradation, the rate constant over Ag@AgCl–PR cubic cages (262.5×10^{-3} min^{-1}) was found to be 28 times larger than the bulk solid Ag@AgCl (9.3×10^{-3} min^{-1}), although both of them had the same process to generate metallic Ag by the PR method. Therefore, it is clearly demonstrated in the current work that having the porous cubic cage morphology can impart enhancement in the photocatalytic activity. Herein the following reasons for this observed high activity of Ag@AgCl cubic cages are suggested. Because cubic cages were composed of six thin-walled squares where both the inner and outer surfaces of the cages were accessible, it attained a large specific surface area for the heterogeneous photocatalytic reactions. The SPR absorption of visible light and the multi-reflection in cavity increased its total absorption efficiency of photon energies. And the metal-semiconductor junction efficiently separates the excited electrons and holes.

As recyclability for photocatalysts is a general requirement for potential application, cyclic bleaching experiments for MO was carried out. Both Ag@AgCl–PR and Ag@AgCl–EGR cubic cages after their first cycle usage (Figure 4a) was collected to carry out subsequent degradation. As seen in Figure 4b, neither Ag@AgCl–PR nor Ag@AgCl–EGR showed significant decrease in their degradation rate after six additional cycles. The trivial lowering of their activity may be due to powder lost during recycling. The XPS results in Figure S6 (Supporting Information) reveal that the Ag@AgCl–PR and Ag@AgCl–EGR samples after six cycles possessed similar compositions with the as-prepared samples. These results demonstrated that the synthesized Ag@AgCl cubic cages remained stable and active for repeated usage. According to previous research, Ag NPs generated on AgCl can generate self-stabilizing mechanism that prevented further destruction of AgCl and maintained its activity.[6a,6d]

2.3. Density Functional Theory Calculations and Finite-Difference Time-Domain Simulation of Ag/AgCl Structures

To provide further insight into the electronic structure of AgCl, the band structure and densities of states (DOS) of AgCl were calculated using density functional theory (DFT). The AgCl unit cell (space group No 225; Fm-3m) is shown in **Figure 5**a. It is known that the functionals such as generalized gradient approximations (GGA), local-density approximation (LDA) within DFT usually undermine the band gap value of semiconductors and

insulators. To obtain an accurate description of the band structure, the calculations were carried out using hybrid DFT functional proposed by Perdew, Burke, and Ernzerhof (PBE0).[17] Figure 5b,c show the band structure and DOS of AgCl calculation results respectively by hybrid PBE0 functional. AgCl material is found to be an indirect bandgap semiconductor. The direct electronic transition is seen at the G point and the indirect transition is seen from R to G point in the band structure (Figure 5b), which explains measured absorption spectrum (two band edges before the 400 nm) of the AgCl sample (Figure 3). It is found that the indirect bandgap value obtained from hybrid functional (PBE0) calculations is 3.61 eV and the direct bandgap value is 5.72 eV (Figure 5b,c), which compare well with the reported literature values of the calculation or experimental results.[6d,18] Both the highly dispersive valence band and conduction band should benefit the transport of the excited charge carriers, which is crucial for high photocatalytic activity. The partial density of states (pDOS) shows that the valence band of AgCl is mainly composed of Cl 3p + Ag 4d, while the conduction band mainly consists of Ag 5s orbitals and a little contribution from Cl 3p. The calculated band structure (Figure 5) and measured optical absorption spectra (Figure 4) indicate the AgCl crystal is inactive under the visible light illumination due to its large band gap. Therefore, the silver nanoparticles should play an important role for the visible light absorption.

It is well known that the electric fields around silver nanoparticles can be enhanced when the incident lights are in the resonance with the localized surface plasmon of silver nanoparticles. To study the role of silver nanoparticles on light enhancement around AgCl crystal, we carried out 3D finite-difference time-domain (FDTD) simulations for silver nanoparticles on AgCl cubes. The calculation results (**Figure 6**a,b) show significant electric filed enhancement near the interface of Ag/AgCl hybrid structure when silver NPs are in plasmon resonances. From the cross-sectional view (Figure 6b), the strongest hot spot is near the Ag/AgCl interface because the refractive index of AgCl (2.1) is much larger than that of water (1.33).[19] The confinement of light near Ag/AgCl is vital to amplify the light absorption of AgCl. We also observed similar electric field distribution pattern for incident wavelength of 400 nm and 800 nm (Figure 6c,d) and particle size of 10 nm, 50 nm, and 100 nm (Figure S8, Supporting Information). For 50 nm Ag sphere, the maximum electric field intensities for different wavelength are in the order of $|E|_{440nm}^2 > |E|_{550nm}^2 > |E|_{800nm}^2$. Therefore, the performance merit of this plasmonic Ag/AgCl hybrid was mainly attributed to the EM field enhancement from 400 to 550 nm. For incident wavelength of 550 nm, the maximum electric filed enhancement was found for 100 nm Ag particles, followed by 50 nm Ag particles, while the field enhancement was least significant for 10 nm Ag particles. It suggests that a larger Ag particle is better for Ag@AgCl photocatalysis, which is consistent with the recent study of Au nanoparticles on TiO_2 surface.[20]

2.4. Ultrafast Electron Transfer Mechanism in Ag@AgCl Structure

To elucidate the underlying mechanism of the superior photocatalytic performance of the Ag@AgCl nanohybrid crystals,

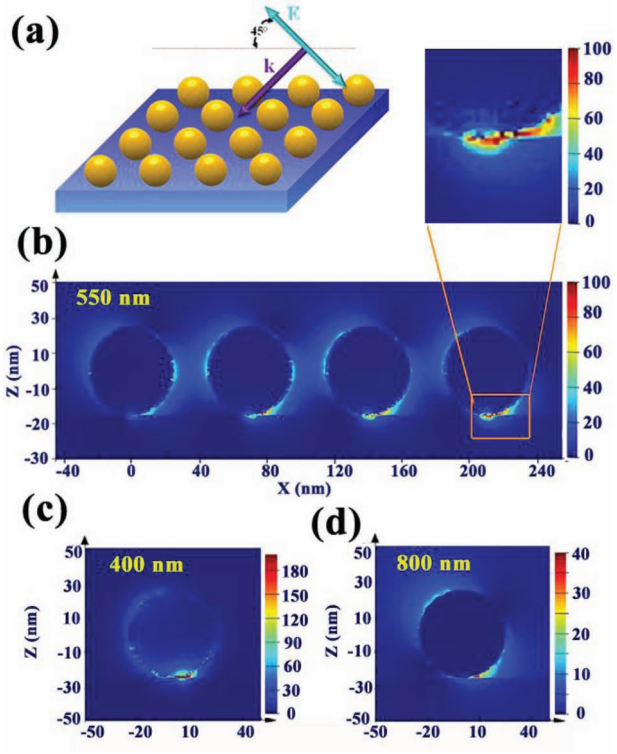

Figure 6. a) The simulation model of the 3D FDTD simulation of a 4 × 4 silver nanospheres array on AgCl substrate excited at 550 nm. b) Side view of the 3D FDTD simulation result. c,d) simulation results of electric field distribution for a single silver nanosphere on AgCl substrate at the incident wavelength of 400 nm and 800 nm respectively. The inset in (a) is the large magnification side-view image of the simulation result of (b).

the photon-induced electron transfer dynamics between them were examined by transient absorption (TA) spectroscopy. TA spectroscopy is a powerful technique for investigating the electron transfer from semiconductor NPs to TiO_2 or other electron acceptors by monitoring the state filling kinetics of the 1s electron level in the semiconductor NPs.[21] For the present study of Ag@AgCl nanohybrid crystals, the free electrons in Ag NPs were selectively excited with 400 nm (3.1 eV) laser pulses. No transient signal was observed on pure AgCl samples under the same excitation conditions, which is consistent with the calculated optical property of AgCl (Figure 5). The photon induced hot electron dynamics were monitored at 470 nm (2.6 eV). The differential transmittance signals for pure Ag NPs are shown in **Figure 7**a,b. The fast decay of the photon-induced-electron-plasmon-bleaching ($\tau_1 \approx 1.8$ ps) was dominated by the electron-electron scattering and electron-phonon scattering (energy transfer from the hot electrons to lattice).[22] The slow recovery of the photon induced absorption transient ($\tau_2 > 2$ ns) to the equilibrium was attributed to the heat dissipation from the Ag NPs to the surrounding matrix (i.e., phonon-phonon interaction). As the sample was measured in vacuum, the observed τ_2 here is much longer than the reported values for Ag NPs in air or in solvents.[22] Figure 7c,d show the case for Ag@AgCl nanohybrid system under the same experimental conditions. The absence of the electron plasmon bleaching and hot electron

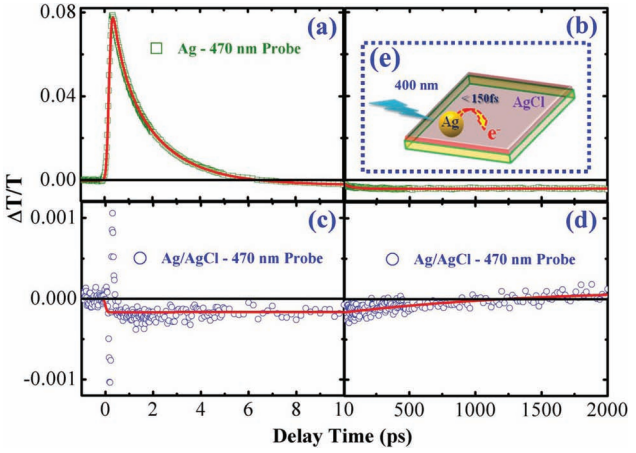

Figure 7. Comparisons of 470 nm transient absorption kinetics of a,b) Ag nanoparticles and c,d) Ag nanoparticles coupled with AgCl nanoparticles after 400 nm excitation. e) Schematic illustration of the ultrafast electron transfer from Ag to AgCl after excitation.

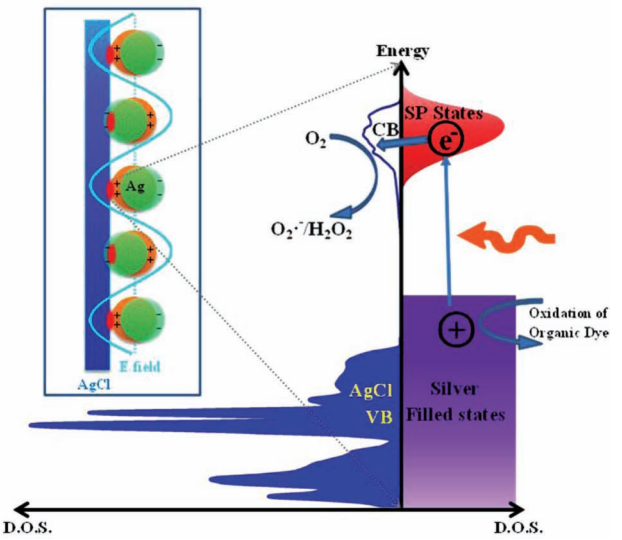

Figure 8. The proposed mechanism of photocatalytic organic dye degradation for the Ag/AgCl hybrid structures.

cooling indicates that there was a strong electronic coupling between the Ag and AgCl conduction bands. The photoinduced energetic electrons in Ag NPs were efficiently injected into AgCl. The injection time was far beyond our TA time resolution (150 fs). Such fast electron injection is consistent with the reported results for strongly electronically coupled semiconductor NPs and TiO_2 (around few fs to tens of fs).[23] Figure 7d clearly shows there was a transition from photo-induced absorption to photo-bleaching (PB) at 1.2 ns for Ag@AgCl nano-hybrid system. Such PB signature arose from the absence of free electrons in Ag NPs. That means the charge separated states can survive till more than a few nanoseconds. This kind of fast built and long lived charge separated states are advantageous to photocatalytic reaction.

Based on the simulation result and TA spectroscopy, the SPR-mediated charge transfer process under the light illumination was proposed, whose scheme is shown in **Figure 8**. A Schottky junction is established at the interface between the silver NPs and AgCl cubes resulting in charge transfer from the AgCl to Ag NPs and a potential barrier of ≈0.8 eV. Upon light irradiation, electromagnetic (EM) wave will be greatly confined and amplified in certain interfacial hot spots (shown as red spots in Figure 8 inset) when the intrinsic frequency of electron oscillation matches with that of the light. The excited surface plasmons rapidly decay, producing many hot electrons, which transiently occupy normally empty state in the silver's conduction band above the Fermi energy. A significant fraction of excited electrons are ultrafast transferred to AgCl. This SPR charge transfer mechanism is analogous to dye sensitization. That is, a dye molecule anchored to a semiconductor acts to absorb light and transfer energetic charge carriers to the semiconductor.[5] For photocatalytic applications, charge transfer plays a central role in the systems where energetic electrons will transfer across the interface to the CB of AgCl, where they can be trapped by O_2 in solution to form $O_2^{\bullet-}$ and H_2O_2, which are reactive species responsible to the destruction of organic molecules. Due to the loss of electrons, the remaining positive charge on the Ag nanoparticles can then contribute to the oxidation of organic dyes (Figure 8).

3. Conclusions

In this work, a novel and economic water soluble sacrificial salt-crystal-template (SCT) process was developed for the large-scale production of hollow Ag@AgCl cage materials that show superior photocatalytic performance compared with the solid form. By using femtosecond transient absorption spectroscopy, we would directly observe plasmon-induced electron transfer from Ag nanoparticles to AgCl surface with ultrafast injection time within 150 fs, contributing to the excellent performance of Ag@AgCl cages toward the photocatalytic application. Also, the reported SCT process opens up a new possibility to fabricate other functional materials with hollow-structures.

4. Experimental Section

Synthesis of Ag@AgCl Cubic Cages: Ag@AgCl cubic cages were synthesized by the water soluble sacrificial salt-crystal-template (SCT) process. In a typical procedure, $AgNO_3$ ethanolic solution was prepared in advance by dissolving $AgNO_3$ (1 mmol) and polyvinylpyrrolidone K40 (PVP, $M_r \approx 40\,000$) (1200 mg) in anhydrous ethanol (20 mL). NaCl saturated aqueous solution was also prepared in advance. After which, NaCl saturated aqueous solution (800 µL) was injected into anhydrous ethanol (100 mL) under stirring, and a white dispersion was formed immediately. Subsequently, $AgNO_3$ ethanolic solution (20 mL) was poured into the NaCl ethanolic dispersion and the mixture was vigorously stirred for 24 h, forming NaCl/AgCl core-shell cubes.

Ag nanoparticles (NPs) were generated on the surface of AgCl by two methods: photo-reduction (PR) and ethylene glycol-assisted reduction (EGR). For photo-reduction method, the NaCl/AgCl ethanolic dispersion was illuminated using solar simulator 300 W Xe lamp (HAL-320, Asahi Spectra Co., Ltd.) for 30 min, forming NaCl/Ag@AgCl–PR core-shell cubes. When the collected NaCl/Ag@AgCl was washed with water, Ag@AgCl–PR was generated. In the EGR method, ethylene glycol (40 mL)

was added to the NaCl/AgCl ethanolic dispersion, which was heated in an oil bath to 160 °C. The solution was maintained at 160 °C for 30 min, and then taken out of oil bath and air-cooled to room temperature, generating Ag@AgCl–EGR. All the processes described above were carried out under vigorous magnetic stirring. For comparison, bulk Ag@AgCl was prepared by the direct reaction between $AgNO_3$ and HCl followed by photo-irradiation (details in Supporting Information). All samples were finally collected after centrifugation, washed with ethanol and deionized water, and dried in an oven at 70 °C.

Sample Characterization: The morphology of the as-synthesized products were investigated by FESEM (JEOL JSM-7600F) and TEM (JEOL JEM-2100F) operating at 200 kV. EDX was carried out in conjunction with the FESEM studies. Phase identification was performed on a Bruker D8 powder X-ray diffractometer with a Cu Kα radiation. The surface properties of prepared samples were characterized by XPS in an Omicron ESCA Probe with a monochromatic Al K_α source at 1486.6 eV. UV-visible diffuse reflectance spectra were recorded on a Shimadzu UV-3600 UV-vis spectrophotometer using $BaSO_4$ as a reference.

Evaluation of Photocatalytic Activity: Methyl orange (MO) was chosen as the target organic compound in this study to probe the photocatalytic performance of various prepared photocatalysts. The batch experiments were conducted with 20 mg of respective photocatalyst suspended in 20 mL of MO aqueous solution (10 mg L^{-1}). The solution was pre-stirred vigorously in the dark for 30 min to establish adsorption-desorption equilibrium, after which a solar simulator 300 W Xe lamp (HAL-320, Asahi Spectra Co., Ltd.) coupled with a super cold filter (YSC0750) that provided visible light with wavelength ranging from 400 nm to 700 nm, was used as the visible light source to irradiate the suspension under vigorous stirring. The light intensity employed was ca. 60 mW cm^{-2}. Aliquots of the suspension at respective irradiation time intervals were collected, centrifuged to remove the photocatalysts, and analysed quantitatively for the absorption peak at 464 nm generated under Shimadzu UV-2501 PC Spectrometer. Respective photocatalysts after the above-mentioned first cycle photocatalysis were centrifuged and collected for subsequent recycling tests. All procedures for the recycling tests are the same as the first cycle.

Electronic Structure Calculations: The electronic structure of AgCl was studied by quantum mechanical calculations within Density Functional Theory framework. All the calculations were done using CASTEP, implemented in the Materials Studio 5.0. The unit cell of AgCl (space group No 225; Fm-3m) was used as stating material and band structure and density of states were plotted after complete geometry optimization. An energy cut-off of 400 eV and monkhorst-pack K-points mesh of 8 × 8 × 8 was used to plot the band structure and density of states. The exchange-correlation functional was constructed by the Generalized Gradient Approximations (GGA) proposed by Perdew, Burke, and Ernzerhof (PBE).[17a] In addition to GGA functional, the hybrid DFT functional proposed by Perdew, Burke, and Ernzerhof (PBE0)[17b] was also used to estimate the band gap values.

Finite-Difference Time-domain (FDTD) Simulation of Ag/AgCl Hybrid Structures: Numerical simulations were done by a 3D FDTD simulation, carried out on a commercial simulation program (FDTD solutions 7.5, Lumerical Solutions, Inc., Vancouver, Canada) to study the intensity and electromagnetic field distribution around Ag/AgCl hybrid structure. Since the nanoscale range silver particles (around 50 nm) were quite randomly distributed on top of AgCl shell (around 1.1 μm), we can approximate the interaction between Ag and AgCl as an ideal model of Ag nanospheres on top of an infinite AgCl substrate. In this calculation, a perfect plane wave with wavelength 550 nm was selected to estimate the interaction between the propagating plane waves and hybrid structures since this specific wavelength was the plasmonic peak position of the Ag nanoparticles according to the UV-vis spectra. The diameter of each Ag nanospheres was 50 nm, and the inter-particle distance was 20 nm. The dielectric constant of silver metal was used from Palik[19] and the refractive index of AgCl was set to be 2.1. The surrounding medium was set to be water with the refractive index of 1.33.

Transient Absorption (TA) Measurement: For femtosecond TA spectroscopy, the laser source was a Coherent Legend regenerative amplifier (150 fs, 1 KHz, 800 nm) that was seeded by a Coherent Mira oscillator (100 fs, 80 MHz). 800 nm wavelength laser pulses were from the regenerative amplifier's output while 400 nm pump pulses were frequency doubled with a BBO crystal. The samples on quartz substrates were kept in vacuum and pumped at 3.1 eV (400 nm) and probed at 2.6 eV (470 nm) which was selected from a white-light continuum. The white light probe pulses (400–750 nm) were generated by focusing a small portion (≈5 μJ) of the fundamental 800 nm laser pulses into a 1 mm-thick sapphire plate. The linear polarization of the pump pulse was adjusted to be perpendicular to that of the probe pulse with a polarizer and a half waveplate. The cross-polarization will help eliminate any contribution from coherent artifacts at early times. Pump-induced changes of transmission ($\Delta T/T$) of the probe beam were monitored using a monochromator/PMT configuration with lock-in detection. The pump beam was chopped at 83 Hz and this was used as the reference frequency for the lock-in amplifier.

Supporting Information

Supporting Information is available from the Wiley Online Library or from the author.

Acknowledgements

Y.T. and Z.J. contributed equally to this work. Y.T. and Z.C. thank the Environment and Water Industry Programme Office (EWI) under the National Research Foundation of Singapore (grant MEWR651/06/160) for the financial support of the work. Z.J. acknowledges the support for this project from CN Yang Scholars Programme of Nanyang Technological University. G.X. and T.C.S. also acknowledge the financial support by NTU start-up grant M58110068, and Singapore National Research Foundation (NRF) through the Singapore Berkeley Research Initiative for Sustainable Energy (SinBeRISE).

Received: November 18, 2012
Revised: December 15, 2012
Published online: January 23, 2013

[1] a) J. D. Bass, C. D. Schaper, C. T. Rettner, N. Arellano, F. H. Alharbi, R. D. Miller, H.-C. Kim, *ACS Nano* **2011**, *5*, 4065; b) Z. G. Yi, J. H. Ye, N. Kikugawa, T. Kako, S. X. Ouyang, H. Stuart-Williams, H. Yang, J. Y. Cao, W. J. Luo, Z. S. Li, Y. Liu, R. L. Withers, *Nat. Mater.* **2010**, *9*, 559; c) K. Maeda, K. Teramura, D. L. Lu, T. Takata, N. Saito, Y. Inoue, K. Domen, *Nature* **2006**, *440*, 295; d) X. Chen, L. Liu, P. Y. Yu, S. S. Mao, *Science* **2011**, *331*, 746; e) M. Liao, J. Feng, W. Luo, Z. Wang, J. Zhang, Z. Li, T. Yu, Z. Zou, *Adv. Funct. Mater.* **2012**, *22*, 3066.

[2] a) Y. Li, Z.-Y. Fu, B.-L. Su, *Adv. Funct. Mater.* **2012**, *22*, 4634; b) S. Yin, Y. Zhang, J. Kong, C. Zou, C. M. Li, X. Lu, J. Ma, F. Y. C. Boey, X. Chen, *ACS Nano* **2011**, *5*, 3831; c) Y. Zhang, Y. Tang, S. Yin, Z. Zeng, H. Zhang, C. M. Li, Z. Dong, Z. Chen, X. Chen, *Nanoscale* **2011**, *3*, 4074; d) Y. Sun, B. Mayers, Y. Xia, *Adv. Mater.* **2003**, *15*, 641.

[3] E. Shimoni, O. Rav-Hon, I. Ohad, V. Brumfeld, Z. Reich, *Plant Cell* **2005**, *17*, 2580.

[4] a) J. B. Joo, Q. Zhang, I. Lee, M. Dahl, F. Zaera, Y. D. Yin, *Adv. Funct. Mater.* **2012**, *22*, 166; b) Y. Tang, P. Wee, Y. Lai, X. Wang, D. Gong, P. D. Kanhere, T.-T. Lim, Z. Dong, Z. Chen, *J. Phys. Chem. C* **2012**, *116*, 2772; c) Y. Zhang, Y. Tang, X. Liu, Z. Dong, H. H. Hng, Z. Chen, T. C. Sum, X. Chen, *Small* **2012**, DOI:10.1002/smll.201202156.

[5] S. Linic, P. Christopher, D. B. Ingram, *Nat. Mater.* **2011**, *10*, 911.
[6] a) P. Wang, B. B. Huang, X. Y. Qin, X. Y. Zhang, Y. Dai, J. Y. Wei, M. H. Whangbo, *Angew. Chem. Int. Ed.* **2008**, *47*, 7931; b) C. Hu, T. W. Peng, X. X. Hu, Y. L. Nie, X. F. Zhou, J. H. Qu, H. He, *J. Am. Chem. Soc.* **2010**, *132*, 857; c) J. G. Yu, G. P. Dai, B. B. Huang, *J. Phys. Chem. C* **2009**, *113*, 16394; d) C. H. An, S. N. Peng, Y. G. Sun, *Adv. Mater.* **2010**, *22*, 2570; e) Y. P. Bi, J. H. Ye, *Chem. Eur. J.* **2010**, *16*, 10327; f) M. S. Zhu, P. L. Chen, M. H. Liu, *ACS Nano* **2011**, *5*, 4529; g) P. Wang, B. B. Huang, Y. Dai, M. H. Whangbo, *Phys. Chem. Chem. Phys.* **2012**, *14*, 9813; h) Y. Tang, Z. Jiang, J. Deng, D. Gong, Y. Lai, H. T. Tay, I. T. K. Joo, T. H. Lau, Z. Dong, Z. Chen, *Acs Appl. Mater. Interfaces* **2012**, *4*, 438; i) Y. X. Tang, V. P. Subramaniam, T. H. Lau, Y. K. Lai, D. G. Gong, P. D. Kanhere, Y. H. Cheng, Z. Chen, Z. L. Dong, *Appl. Catal. B-Environ.* **2011**, *106*, 577; j) Y. Tang, Z. Jiang, Q. Tay, J. Deng, Y. Lai, D. Gong, Z. Dong, Z. Chen, *RSC Adv.* **2012**, *2*, 9406; k) M. S. Zhu, P. L. Chen, M. H. Liu, *Langmuir* **2012**, *28*, 3385; l) X. F. Zhou, C. Hu, X. X. Hu, T. W. Peng, J. H. Qu, *J. Phys. Chem. C* **2010**, *114*, 2746; m) Z. Lou, B. Huang, X. Ma, X. Zhang, X. Qin, Z. Wang, Y. Dai, Y. Liu, *Chem. Eur. J.* **2012**, *18*, 16090; n) P. Wang, B. Huang, Z. Lou, X. Zhang, X. Qin, Y. Dai, Z. Zheng, X. Wang, *Chem. Eur. J.* **2010**, *16*, 538.
[7] A. Takai, P. V. Kamat, *ACS Nano* **2011**, *5*, 7369.
[8] B. Wiley, Y. G. Sun, B. Mayers, Y. N. Xia, *Chem. Eur. J.* **2005**, *11*, 454.
[9] a) Y. G. Sun, *J. Phys. Chem. C* **2010**, *114*, 2127; b) S. H. Im, Y. T. Lee, B. Wiley, Y. Xia, *Angew. Chem. Int. Ed.* **2005**, *44*, 2154.
[10] J. Jiang, L. Zhang, *Chem. Eur. J.* **2011**, *17*, 3710.
[11] H. Cheng, B. Huang, P. Wang, Z. Wang, Z. Lou, J. Wang, X. Qin, X. Zhang, Y. Dai, *Chem. Commun.* **2011**, *47*, 7054.
[12] X. Chen, Z. Zheng, X. Ke, E. Jaatinen, T. Xie, D. Wang, C. Guo, J. Zhao, H. Zhu, *Green Chem.* **2010**, *12*, 414.
[13] Y. Li, Y. Ding, *J. Phys. Chem. C* **2010**, *114*, 3175.
[14] a) Y.-K. Lai, J.-Y. Huang, H.-F. Zhang, V.-P. Subramaniam, Y.-X. Tang, D.-G. Gong, L. Sundar, L. Sun, Z. Chen, C.-J. Lin, *J. Hazard. Mater.* **2010**, *184*, 855; b) Q. Xiang, J. Yu, B. Cheng, H. C. Ong, *Chem. Asian. J.* **2010**, *5*, 1466.
[15] a) K. L. Kelly, E. Coronado, L. L. Zhao, G. C. Schatz, *J. Phys. Chem. B* **2002**, *107*, 668; b) A. Moores, F. Goettmann, *New J. Chem.* **2006**, *30*, 1121; c) L. Jiang, Y. Tang, C. Liow, J. Wu, Y. Sun, Y. Jiang, Z. Dong, S. Li, V. P. Dravid, X. Chen, *Small* **2012**, doi:10.1002/smll.201202561.
[16] P. K. Jain, K. S. Lee, I. H. El-Sayed, M. A. El-Sayed, *J. Phys. Chem. B* **2006**, *110*, 7238.
[17] a) J. P. Perdew, K. Burke, M. Ernzerhof, *Phys. Rev. Lett.* **1996**, *77*, 3865; b) C. Adamo, V. Barone, *J. Chem. Phys.* **1999**, *110*, 6158.
[18] S. Glaus, G. Calzaferri, *Photochem. Photobiol. Sci.* **2003**, *2*, 398.
[19] E. D. Palik, *Handbook of Optical Constants of Solids*, Elsevier Science, Burlington **1997**
[20] Z. W. Seh, S. Liu, M. Low, S.-Y. Zhang, Z. Liu, A. Mlayah, M.-Y. Han, *Adv. Mater.* **2012**, *24*, 2310.
[21] a) T. Hirakawa, P. V. Kamat, *J. Am. Chem. Soc.* **2005**, *127*, 3928; b) I. Robel, M. Kuno, P. V. Kamat, *J. Am. Chem. Soc.* **2007**, *129*, 4136; c) J. Tang, J. R. Durrant, D. R. Klug, *J. Am. Chem. Soc.* **2008**, *130*, 13885.
[22] a) O. L. Muskens, N. Del Fatti, F. Vallée, *Nano Lett.* **2006**, *6*, 552; b) H. Inouye, K. Tanaka, I. Tanahashi, K. Hirao, *Phys. Rev. B* **1998**, *57*, 11334.
[23] a) W. A. Tisdale, K. J. Williams, B. A. Timp, D. J. Norris, E. S. Aydil, X. Y. Zhu, *Science* **2010**, *328*, 1543; b) J. B. Sambur, T. Novet, B. A. Parkinson, *Science* **2010**, *330*, 63.